
The soft X-ray background with Suzaku: I. Milky Way halo

Masaki UEDA¹, Hayato SUGIYAMA¹, Shogo B. KOBAYASHI¹, Kotaro FUKUSHIMA¹, Noriko Y. YAMASAKI², Kosuke SATO³, and Kyoko MATSUSHITA^{1,*}

¹Department of Physics, Tokyo University of Science, 1-3 Kagurazaka, Shinjuku-ku, Tokyo 162-8601 Japan

²Institute of Space and Astronautical Science, Japan Aerospace Exploration Agency, 3-1-1 Yoshinodai, Chuo-ku, Sagami-hara, Kanagawa 252-5210, Japan

³Graduate School of Science and Engineering, Saitama University, 255 Shimo-Okubo, Sakura-ku, Saitama, Saitama 338-8570, Japan

*E-mail: matusita@rs.tus.ac.jp

Received 2022 June 13; Accepted 2022 September 4

Abstract

We present measurements of the soft X-ray background emission for 130 Suzaku observations at $75^\circ < l < 285^\circ$ and $|b| > 15^\circ$ obtained from 2005 to 2015, covering nearly one solar cycle. In addition to the standard soft X-ray background model consisting of the local hot bubble and the Milky Way Halo (MWH), we include a hot collisional-ionization-equilibrium component with a temperature of ~ 0.8 keV to reproduce spectra of a significant fraction of the lines of sight. Then, the scatter in the relation between the emission measure vs. temperature of the MWH component is reduced. Here, we exclude time ranges with high count rates to minimize the effect of the solar wind charge exchange (SWCX). However, the spectra of almost the same lines of sight are inconsistent. The heliospheric SWCX emissions likely contaminate and gives a bias in measurements of temperature and the emission measure of the MWH. Excluding the data around the solar maximum and using the data taken before the end of 2009, at $|b| > 35^\circ$ and $105^\circ < l < 255^\circ$, the temperature (0.22 keV) and emission measure ($2 \times 10^{-3} \text{ cm}^{-6} \text{ pc}$) of the MWH are fairly uniform. The increase of the emission measure toward the lower Galactic latitude at $|b| < 35^\circ$ indicates a presence of a disk-like morphology component. A composite model which consists of disk-like and spherical-morphology components also reproduces the observed emission measure distribution of MWH. In this case, the hydrostatic mass at a few tens of kpc from the Galactic center agrees with the gravitational mass of the Milky Way. The plasma with the virial temperature likely fills the Milky Way halo in nearly hydrostatic equilibrium. Assuming the gas metallicity of 0.3 solar, the upper limit of the gas mass of the spherical component out to 250 kpc, or the virial radius, is \sim a few $\times 10^{10} M_\odot$.

Key words: Galaxy:halo — X-rays:ISM — X-rays:diffuse background — ISM:structure

1 Introduction

Galaxies are thought to be surrounded by an extended gaseous halo, the circumgalactic medium (CGM), which is

expected to contain a significant fraction of the baryonic mass (e.g. Tumlinson et al. 2017 and references therein). Under the cold dark matter cosmology, galaxies grow by accretion of matter from their surroundings. The accreting gas is expected to be heated to the virial temperature by shock waves generated by mass accretion (e.g., Rees & Ostriker 1977) and fills the halo of galaxies in nearly hydrostatic equilibrium. In addition, supernovae (SNe) heat the interstellar medium and sometimes cause an outflow toward intergalactic space. Therefore, the observations of hot gas in galaxies are essential to study the structure formation of the Universe and feedback from galaxies to intergalactic space. Suzaku, Japan's X-ray astronomy satellite, is characterized by its low background, enabling us to detect low-surface brightness X-ray emissions from hot gas in the Milky Way.

The soft X-ray background detected below ~ 1 keV is thought to mainly come from the hot gas in and around the Milky Way (e.g., Snowden et al. 1998, Kuntz & Snowden 2000). The X-ray spectrum of the soft X-ray background is usually modeled with a sum of collisional-ionization-equilibrium (CIE) plasmas of 0.1 keV and 0.2–0.3 keV. A cavity surrounding the sun filled with CIE plasma with a temperature of 0.1 keV is called the Local Hot Bubble (LHB). The Milky Way Halo (MWH) component, hot gas with a temperature of 0.2–0.3 keV, probably comes from a more extended, diffuse plasma. The emission measure of the MWH component varies by over an order of magnitude, even toward the Galactic anticenter (Henley & Shelton 2013, Nakashima et al. 2018). The detection of absorption lines of O VII and O VIII in the X-ray spectra of active galactic nuclei (e.g. Nicastro et al. 2002, Fang et al. 2003, Hagihara et al. 2010) confirmed the presence of 0.2–0.3 keV plasma around the Milky Way. In addition, Yoshino et al. (2009), Henley & Shelton (2013), Sekiya et al. (2014a), Nakashima et al. (2018), Gupta et al. (2021), Gupta et al. (2022) reported "excess" emissions which can be modeled by a plasma with supersolar Ne/Fe ratio or a higher temperature component (0.5–0.9 keV) from several lines of sight.

Heliospheric and geocoronal solar wind charge exchange (SWCX) emissions sometimes contaminate the soft X-ray emissions from outside the solar system. The SWCX emission is caused by interaction between the solar wind ions and neutral atoms (e.g. Cravens et al. 2001, Koutroumpa et al. 2007). In some cases, highly time-variable strong emission lines of C, O, Ne, and Mg possibly caused by geocoronal SWCX were detected with XMM-Newton (e.g. Carter et al. 2010) and Suzaku (e.g. Fujimoto et al. 2007, Ishi et al. 2019). These emissions can be filtered using light curves in the soft energy band and ion flux measure-

ments of the solar wind. The time variation of the heliospheric SWCX should be much slower, and its intensity is expected to relate to the solar cycle. Yoshitake et al. (2013) studied O VII line intensity toward the Lockman hole observed with Suzaku from 2006 and 2011. After screening the geocoronal SWCX emissions using the soft-band light curve and proton flux of the solar wind, they found an O VII line enhancement possibly related to the heliospheric SWCX. Qu et al. (2022) measured the O VII and O VIII line strengths using the XMM data from 2000 to 2010 and studied the correlation with the solar activity. They concluded that the heliospheric SWCX emissions significantly (30–50 %) contaminate these O lines in average. In addition to the SWCX components, Suzaku data was contaminated with the strong O I $K\alpha$ line scattered by the earth's atmosphere around the solar maximum (Sekiya et al. 2014b).

In this study, we present data analysis of 130 observations with Suzaku at $75^\circ < l < 285^\circ$ and at $|b| > 15^\circ$ excluding the Galactic center and the Galactic plane to study the distribution of the hot gas which fills the Milky Way halo. Here, l is the Galactic longitude, and b is the Galactic latitude. These data were obtained from 2005 to 2015, covering nearly one solar cycle. Some regions are observed multiple times and therefore suitable for studying the contaminations by SWCX. In Section 2, we describe the observations and data reduction. The spectral analysis and results are presented in Section 3. We present the results of spectral fittings with an extra hot CIE component with a temperature of 0.8 keV. This paper mainly shows the temperatures and emission measures of the MWH component. Those of the 0.8 keV component will be presented in another paper (Sugiyama et al. in preparation). We discuss and summarize the results in Sections 4 and 5, respectively. This paper uses the solar abundance table by Lodders (2003). Errors are reported at the 68% confidence level unless otherwise stated.

2 Observations and data reduction

We analyzed archival Suzaku/XIS data of 130 observations toward $75^\circ < l < 285^\circ$ and $|b| > 15^\circ$. The observation log is shown in Appendix. Here, we excluded regions around extended objects, such as clusters of galaxies and supernova remnants. The observations around very bright point sources are also excluded. The sample includes ten data toward Lockman Hole from 2005 to 2014, six data toward the North ecliptic pole (NEP) obtained in 2005, 2006, and 2009, and four data toward the South ecliptic pole (SEP) observed in 2009. The pointing position of the Lockman Hole observation in 2005 is offset by 0.5° from the other

Lockman Hole observations. Those of NEP in 2005 and 2006 are nearly identical, but the other four are offset by $\sim 1.2^\circ$. These observations with almost the same sightlines are suitable to constrain contaminating emissions caused by solar activity.

The XIS has four CCD sensors: XIS0, 2, and 3 contain front-illuminated (FI) CCDs and XIS1 has a back-illuminated (BI) CCD (Koyama et al. 2007). The Suzaku/XIS detectors are sensitive in the 0.4–10 keV energy band with the field of view (FOV) of $\sim 18' \times 18'$. We analyzed the data of the four CCDs taken before the XIS2 loss in November 2006. After the loss, we analyzed the data of the three remaining CCDs. We used data with normal clocking mode with no window option. Data obtained with 3×3 and 5×5 editing modes were merged, and the standard filtering procedures (Earth elevation $> 10^\circ$, cutoff rigidity > 6 GeV/c) were applied. Additional flickering pixels¹ were removed.

To remove point sources in the XIS FOVs, we created images in the 0.5–2.0 keV and 2.0–5.0 keV energy bands and applied the *wavdetect* tool in the CIAO package. From the subsequent analysis, we excised circular regions around the point source candidates with a significance of $> 3\sigma$. For sources with a flux lower than 5.0×10^{-14} erg s $^{-1}$ cm $^{-2}$ in the energy band of 0.5–5.0 keV, we excised the circular region centered on each source with a radius of $1'$. For brighter sources, this radius is not enough to exclude scattered photons by the X-ray telescopes of Suzaku. For example, two stars emit strong Fe-L lines, numbered 8 and 10 in figure 1, in the FOV of the Lockman hole observation in 2005. Scattered photons from these stars strongly contaminate the spectra when the exclusion radius is $1'$. Therefore, for each brighter source, we determined the exclusion radius based on its flux in the 0.5–7.0 keV band. For example, the exclusion radii for the flux of 1.0×10^{-13} erg s $^{-1}$ cm $^{-2}$ and 5.0×10^{-12} erg s $^{-1}$ cm $^{-2}$ are $1'.5$ and $4'.5$, respectively. For sources with a power-law spectrum of a photon index of 1.7, these radii correspond to the flux level of scattered photons from the point source is half of the background. Further increasing the exclusion radii did not change the results.

To decrease the contamination caused by the SWCX and other background fluctuations, we created light curves and excluded the time ranges when the count rate exceeds 3σ . To increase the available exposure time, we have not adopted any further filtering using the proton flux of the solar wind to reduce the effect of the SWCX or using elevation angle from the sunlit Earth's limb for suppressing contamination by the O I emission from the Earth's atmosphere. The screening criteria used in this work are similar

¹ http://www.astro.isas.ac.jp/suzaku/analysis/xis/nxb_new2/

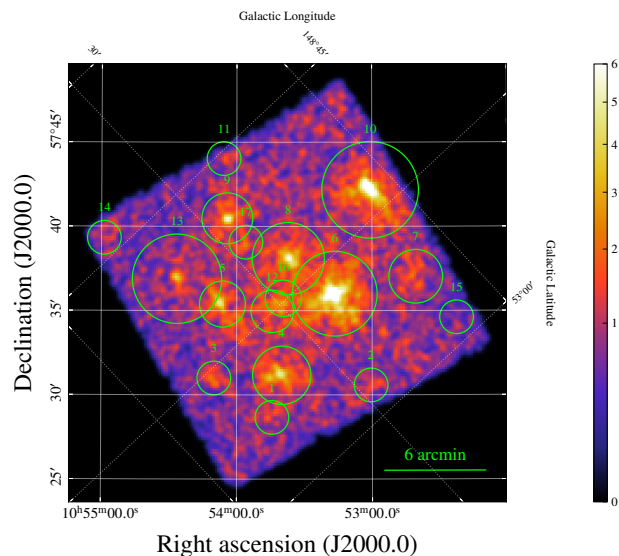


Fig. 1. The XIS1 image (0.5–5.0 keV) of Lockman Hole (OBSID:100046010) observed in 2005. The circular regions with numbers are excluded from the spectral analysis.

to those used to study low-surface brightness targets and, therefore, suitable to study the effects of the systematic uncertainties in other data obtained with Suzaku.

3 Spectral analysis and results

We extracted a spectrum over the FOV of each XIS detector of each observation. To create ancillary response files (ARFs), we used the *xissimarfgen* ftools task (Ishisaki et al. 2007) assuming uniform emission from a circular region with a radius of $20'$. The effects of contaminants and the optical blocking filter of XISs were included in the ARFs. We used the *xismfgen* ftools task to create the redistribution matrix files (RMFs). The instrumental background, or non-X-ray background (NXB), was estimated from the night-Earth database using the *xisnxbgen* ftools task (Tawa et al. 2008). We used XSPEC version 12.10.1b to model the NXB-subtracted spectra. Unless otherwise stated, we used energy ranges of 0.4–7.0 keV for the BI spectra, and 0.5–7.0 keV for the FI spectra. We rebinned each spectrum to a minimum of one count per bin and employed the extended C-statistic (Cash 1979). We used APEC (Astrophysical Plasma Emission Code, Smith et al. 2001, Foster et al. 2012) with AtomDB version 3.0.9 to model a CIE plasma.

3.1 Stacked Spectra of the 130 observations

To study possible emission components of the soft X-ray background, we created stacked XIS-FI (XIS0, 2, 3) and XIS-BI (XIS1) spectra of the 130 observations. We first tried a spectral fitting with a model which consists of four

components: the cosmic X-ray background (CXB), two CIE components (*apec* model in XSPEC) to model the LHB (and SWCX) and MWH, and the O I $K\alpha$ line for the scattered photon from the sunlit atmosphere of the Earth. Hereafter, we denote this model as Model-s. We adopted a power-law model with a photon index of 1.4 to model the CXB component. The emission from the heliospheric SWCX and LHB are empirically modeled with an unabsorbed CIE component of $kT \sim 0.1$ keV with the solar metallicity (e.g. Fujimoto et al. 2007, Yoshino et al. 2009, Henley & Shelton 2013, Nakashima et al. 2018). We also fixed the temperature of the LHB component at 0.1 keV and the abundances of the LHB and MWH components at 1 solar. The CXB and the MWH components are subject to photoelectric absorption due to cold gas, and we modeled this absorption using the *phabs* model in the XSPEC spectral fitting tool. A Gaussian at fixed central energy of 0.525 keV was used to model the O I line. The normalization of each component was allowed to vary. Hereafter, we call the temperature and emission measure ($\int n_e n_H ds$) of the MWH component as kT_{halo} and EM_{halo} , respectively. Here, s is the distance along the line of sight.

We fitted the stacked BI and FI spectra simultaneously with Model-s. Here, we used energy ranges of 0.5–7.0 keV and 0.6–7.0 keV for the BI and FI spectra, respectively, since stacking may cause some problems in the lower energy band due to stacking spectra with different column densities of the contamination and the Galactic absorption. Since there is a slight discrepancy between the stacked FI and BI spectra in the lower energy band, we allowed the N_{H} for the two spectra to vary separately. The result of the spectral fitting with Model-s is shown in table 1 and the stacked BI spectrum and the best-fit model are shown in figure 2. This fit cannot reproduce the spectra with a C-statistics/d.o.f of 6843/3524 and there remain clear residual structures at 0.7–1 keV.

To reproduce the residual structures, we added five Gaussians to Model-s. Here, the line widths of these Gaussians were fixed at 0. We fixed the line energy of a Gaussian at 0.561 keV, which corresponds to the forbidden line of O VII He α . Hereafter, we call this model Model-g. The derived C-statistics, 5608, is significantly better than that for Model-s. This model can reproduce the observed line-like structures relatively well (table 1, figure 2). The best-fit kT_{halo} , 0.22 keV, is close to those derived with Model-s. The best-fit energies of the other additional Gaussians are 0.86 keV, 0.93 keV, 1.04 keV, and 1.31 keV. These energies are close to those of O VIII 6p to 1s line at 0.847 keV, the forbidden line of Ne IX He α at 0.905 keV, Ne X Ly α at 1.022 keV, and the forbidden line of Mg XI He α line at 1.331 keV, respectively.

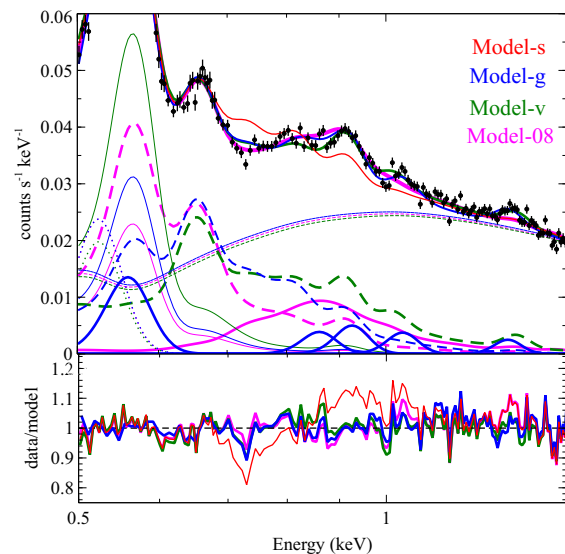


Fig. 2. The stacked XIS1 spectra (top) and data-to-model ratio (bottom) fitted with Model-s (red), Model-g (blue), Model-v (green), and Model-08 (magenta). The contributions of MWH (thick dashed lines), LHB (thin solid lines), CXB (thin dashed lines), and O I (thin dotted lines) components for Model-g, Model-v, and Model-08 are shown. The thick magenta solid line corresponds to the 0.8 keV component for Model-08, and the thick blue solid lines are additional Gaussians for Model-g.

Yoshino et al. (2009) and Nakashima et al. (2018) tried a variable abundance CIE model for the MWH component. They sometimes got a very high Ne abundance to explain the 0.9 keV peak in some spectra. We then replaced the *apec* model for the MWH component of the Model-s with *vapec* model (hereafter Model-v) and fitted the stacked spectra in the same way. The abundances of O, Ne, Mg, and Fe were allowed to vary, and those of the other elements were fixed at 1 solar. The result is shown in table 1 and figure 2. The derived C-statistics, 5421, is slightly better than that with Model-g. kT_{halo} increased to 0.33 keV, and the abundances of O, Ne, and Mg are around 0.8–0.9 solar, while the Fe abundance is only 0.2 solar.

Yoshino et al. (2009) also tried a spectral fitting model with an additional CIE component with a temperature of 0.6–1 keV to reproduce the 0.9 keV peak. Therefore, we added another *apec* component (hereafter 0.8 keV component) modified by the photoelectric absorption to Model-s and fitted the spectrum. Hereafter, we call this model Model-08. Here, the metal abundance was fixed at 1 solar. The derived C-statistics, 5511, is also much smaller than that with Model-s. The best-fit temperature of the additional *apec* component is 0.76 keV, and kT_{halo} decreases to 0.18 keV. As shown in figure 2, Model-08 gives a better fit than Model-v below 1 keV, although it fails to produce the line-like structures at 1.0 keV and 1.3 keV, which cor-

Table 1. Fitting results of the stacked spectra

	Model-s	Model-g	Model-v	Model-08
EM_{LHB}^*	2.3×10^{-2}	$(1.3 \pm 0.2) \times 10^{-2}$	$(2.7 \pm 0.1) \times 10^{-2}$	$(1.1 \pm 0.1) \times 10^{-2}$
kT_{halo} (keV)	0.24	$0.219^{+0.001}_{-0.001}$	0.333 ± 0.007	0.175 ± 0.003
EM_{halo}^*	2.9×10^{-3}	$(3.4 \pm 0.1) \times 10^{-3}$	$(3.6 \pm 0.5) \times 10^{-3}$	$(5.7 \pm 0.3) \times 10^{-3}$
MWH: O (solar)	1.0 (fix)	1.0 (fix)	$0.91^{+0.19}_{-0.14}$	1.0 (fix)
MWH: Ne (solar)	1.0 (fix)	1.0 (fix)	$0.81^{+0.15}_{-0.11}$	1.0 (fix)
MWH: Mg (solar)	1.0 (fix)	1.0 (fix)	$0.78^{+0.13}_{-0.10}$	1.0 (fix)
MWH: Fe (solar)	1.0 (fix)	1.0 (fix)	$0.21^{+0.04}_{-0.03}$	1.0 (fix)
O I Normalization [†]	1.7	1.72 ± 0.05	1.50 ± 0.07	1.80 ± 0.05
N_{H} (10^{20}cm^{-2}) for FI	0.0	0.0 (< 0.1)	0.0 (< 0.1)	0.0 (< 0.1)
N_{H} (10^{20}cm^{-2}) for BI	2.6	2.4 ± 0.3	3.3 ± 0.3	2.6 ± 0.3
CXB norm [‡]	8.7	8.55 ± 0.03	8.44 ± 0.03	8.46 ± 0.03
$kT_{0.8 \text{keV}}$ (keV)	—	—	—	0.76 ± 0.01
$EM_{0.8 \text{keV}}^*$	—	—	—	$(4.6 \pm 0.2) \times 10^{-4}$
Gaussian Energy (keV)	—	0.561 (fix)	—	—
Normalization [†] of O VII He α	—	1.95 ± 0.36	—	—
Gaussian Energy (keV)	—	0.863 ± 0.007	—	—
Normalization [†] of O VIII 6p to 1s? Fe?	—	0.14 ± 0.01	—	—
Gaussian Energy (keV)	—	0.929 ± 0.005	—	—
Normalization [†] of Ne IX He α ? Fe?	—	0.16 ± 0.01	—	—
Gaussian Energy (keV)	—	1.040 ± 0.003	—	—
Normalization [†] of Ne X Ly α ?	—	0.11 ± 0.01	—	—
Gaussian Energy (keV)	—	1.315 ± 0.006	—	—
Normalization [†] of Mg XI He α ?	—	0.063 ± 0.004	—	—
C-Statistics/d.o.f	6843/3524	5608/3515	5421/3520	5511/3522

* Emission measure (integrated over the line of sight, $\int n_e n_H ds$) in units of $\text{cm}^{-6} \text{pc}$.

† Normalization of Gaussian in units of photons $\text{cm}^{-2} \text{s}^{-1} \text{sr}^{-1}$ (LU)

‡ Normalizations at 1 keV for the CXB component in units of photons $\text{cm}^{-2} \text{s}^{-1} \text{keV}^{-1} \text{sr}^{-1}$.

respond to the energy of Ne Ly α and Mg He α , respectively.

3.2 Spectral fitting of the individual observations

We then fitted the XIS spectra of the individual observations with Model-s and Model-08. Since the Model-v fits for the individual observations give similar results to those obtained by Nakashima et al. (2018), we do not present the results in this paper.

3.2.1 The standard model

We fitted the XIS spectra of the individual observations with Model-s. Photoelectric absorption by cold gas in our Galaxy was modeled using *phabs* with a fixed hydrogen column density at the value by Kalberla et al. (2005). The left panel of figure 3 shows the scatter plot of EM_{halo} vs. kT_{halo} . In most cases, kT_{halo} and EM_{halo} are in the range 0.15–0.3 keV and $(1\text{--}30) \times 10^{-3} \text{cm}^{-6} \text{pc}$, respectively, and inversely correlated. As reported by Yoshino et al. (2009), Sekiya et al. (2014a), and Nakashima et al. (2018), some observations show significantly higher kT_{halo} around 0.5–0.8 keV. We find that observations with almost the same or nearby pointings show significantly different kT_{halo} and

EM_{halo} . For example, the nine Lockman Hole data obtained from 2006 to 2014 have almost the same sightlines. However, their kT_{halo} and EM_{halo} are not consistent with each other and span similar ranges to those of the other observations. EM_{halo} of the NEP observations in 2009, which point 1.2° offset from those in 2005 and 2006, are significantly lower than those derived for NEP in 2005 and 2006.

3.2.2 The spectral model with a hot component

We then fitted the spectra of each observation with Model-08 but fixed the temperature of the hottest *apex* component at 0.8 keV. As shown in figure 4, Model-08 gives consistent or better fits than Model-s. With Model-08, among 130 observations, 56 of them got $\Delta C < -9$ compared to those with Model-s. Here, ΔC is the difference in C statistic between the two models. The results of the emission measure of the 0.8 keV component will be presented in Sugiyama et al. in preparation. With Model-08, as shown in the right panel of figure 3 and table 2, EM_{halo} spans an order of magnitude: the median value is $4.0 \times 10^{-3} \text{cm}^{-6} \text{pc}$ and the 16th–84th percentile range is $(1.6\text{--}10) \times 10^{-3} \text{cm}^{-6} \text{pc}$. The median and the 16th–84th percentile range of kT_{halo} are 0.19 keV

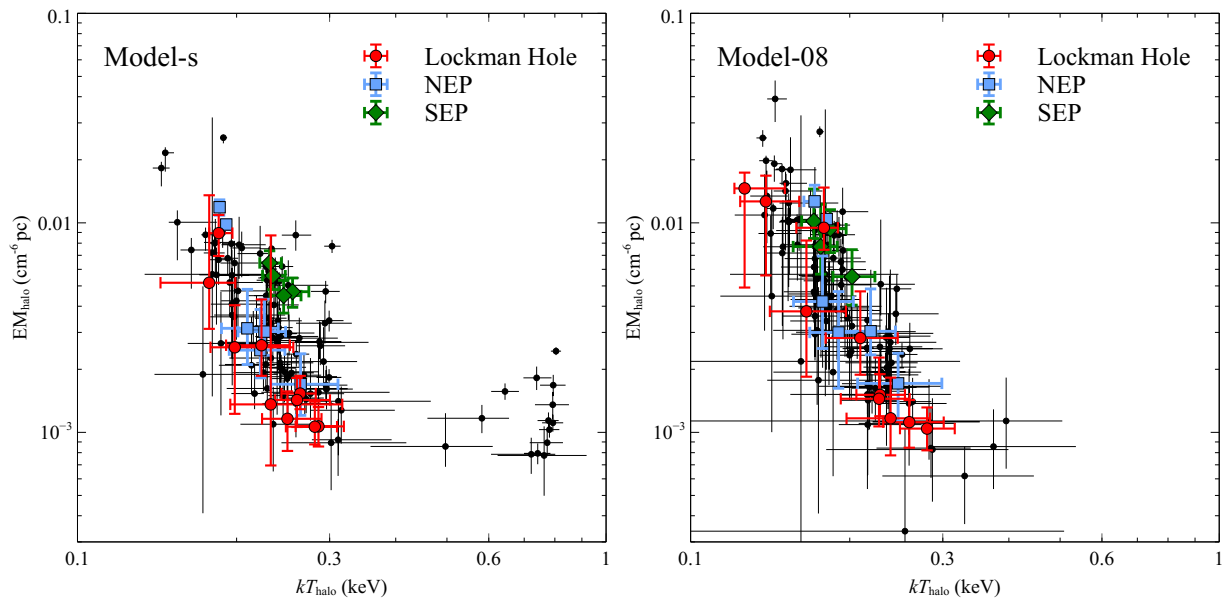


Fig. 3. EM_{halo} against kT_{halo} with Model-s (left) and Model-08 (right). The filled circles, filled squares, and filled diamonds correspond to the Lockman hole, NEP, and SEP, respectively.

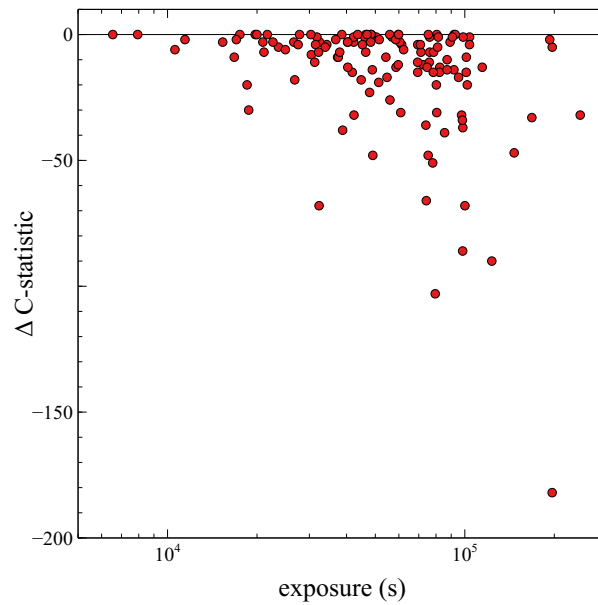


Fig. 4. C-statistics for each observation derived from Model-08 subtracted by that from Model-s, Δ C-statistic, plotted against exposure time.

and 0.15–0.23 keV, respectively. kT_{halo} and EM_{halo} show a clear inverse correlation with a much smaller scatter than that for Model-s. When we divide the sample into two subsamples with $kT_{\text{halo}} = 0.19$ keV, the median values of EM_{halo} differ by a factor of ~ 4 (table 2). Again, those of the Lockman Hole observations with almost the same sightline span similar ranges to the other observations and are inconsistent with each other.

3.3 Correlations with the solar activity

Suzaku was operated from 2005 to 2015, covering nearly one solar cycle, including the solar minimum around 2009 and the solar maximum around 2014. Yoshitake et al. (2013) found that the MWH emission measure depends on the solar activity using the Lockman hole data from 2006 to 2011 obtained with Suzaku. The discrepancy among the observations with almost the same lines of sight indicates the existence of time-variable emission. In figure 5, we plot kT_{halo} , EM_{halo} , emission measures of LHB, and normalizations of the O I line with Model-08 against observation date with the 13-month smoothed sunspot number². kT_{halo} tend to be higher than 0.2 keV (the median value is 0.22 keV) before the end of 2009, while most of them are lower than 0.2 keV (the median value is 0.17 keV) after 2010. As shown in figure 5, the Lockman Hole data obtained in 2012–2015 also show much higher EM_{halo} than those obtained in 2006–2010. Most of EM_{halo} of the 130 observations show a similar trend to those of the Lockman Hole. When we divide the data taken before and after the end of 2009 (hereafter 2005–2009 data and 2010–2015 data, respectively), the scatters are relatively small, as shown in table 2.

The time dependence of EM_{halo} resembles the 13-month smoothed sunspot number. Therefore, in figure 6, we plot kT_{halo} , EM_{halo} , emission measures of LHB, and normalizations of the O I line with Model-08 against the 13-month smoothed sunspot number. The medians and the 16th–84th percentile ranges of different sunspot numbers are summarized in table 2. For the data taken at the sunspot number is less than 20, kT_{halo} and EM_{halo} are rather uniform, with their median values are 0.22 keV and $2.1 \times 10^{-3} \text{ cm}^{-6}\text{pc}$, respectively. In contrast, for data taken at the sunspot numbers are larger than several tens, EM_{halo} increases dramatically.

As found by Sekiya et al. (2014b), the brightness of the O I line increases after the solar minimum around 2009 (Figure 5). In contrast, the emission measure of the LHB does not show a significant dependence on the observation date or 13-month smoothed sunspot number (figures 5 and

6).

3.4 Time variable emission components with the Lockman Hole observations

Figure 7 shows the ratios of the XIS1 spectra of the Lockman Hole obtained from 2009 to 2014 to the best-fit model of the 2009 observation with Model-08. After the solar minimum around 2009, there is an enhancement at 0.56 keV which corresponds to O VII He α . There is a weaker peak at O VIII Ly α (0.65 keV) in the 2013 spectrum. In addition, a strong peak at 0.525 keV of the O I line is seen in the spectra obtained in 2013.

We fitted the XIS1 spectra of Lockman Hole obtained from 2006 to 2014 simultaneously with Model-08, but we added two Gaussians at the fixed energies at O VII He α (0.56 keV) and O VIII Ly α (0.65 keV). The normalizations of the additional Gaussians are fixed at zero for the 2009 spectrum while allowed to vary for the others. The temperature of the MWH and 0.8 keV components were fixed at 0.22 keV and 0.80 keV, respectively and the normalizations of LHB, MWH, and the 0.8 keV component were assumed to have the same values. This model yields a good fit with a C-statistic/d.o.f of 11937/11305. Although there is a hint of excess at 0.85 keV (O VIII 6p to 1s) in the spectra of 2013, when we added one more Gaussian to the model, its significance is less than 2σ .

Figure 8 shows the excess line intensities of the O VII He α , O VIII Ly α , and O I compared to the 2009 spectrum plotted against the observation date. The intensities of the excess O VII line increased from the solar minimum in 2009 to the solar maximum in 2014. Figure 8 also compares the excess line strengths of the O VII line compared to the 2009 data obtained by Yoshitake et al. (2013). Our excess O VII line strength for the 2010 observation agrees well with the value derived by Yoshitake et al. (2013), although our screening criteria are not severe. In contrast, our excess O VII line strength for the 2011 data is lower than that obtained by Yoshitake et al. (2013), since their model did not include the O I line component. The excess O VIII line strengths are much weaker than those of the O VII line. We detected the O VIII line with $> 3\sigma$ significance only in 2013, where its intensity is about 20% of that of the O VII line. As found by Sekiya et al. (2014a), the O I line is very bright around the solar maximum in 2014.

4 Discussion

4.1 Emission related to the solar activity

To study the soft X-ray background emission, we analyzed 130 Suzaku observations, covering nearly one solar cycle,

² <<http://www.sidc.be/silso/dayssnplot>>

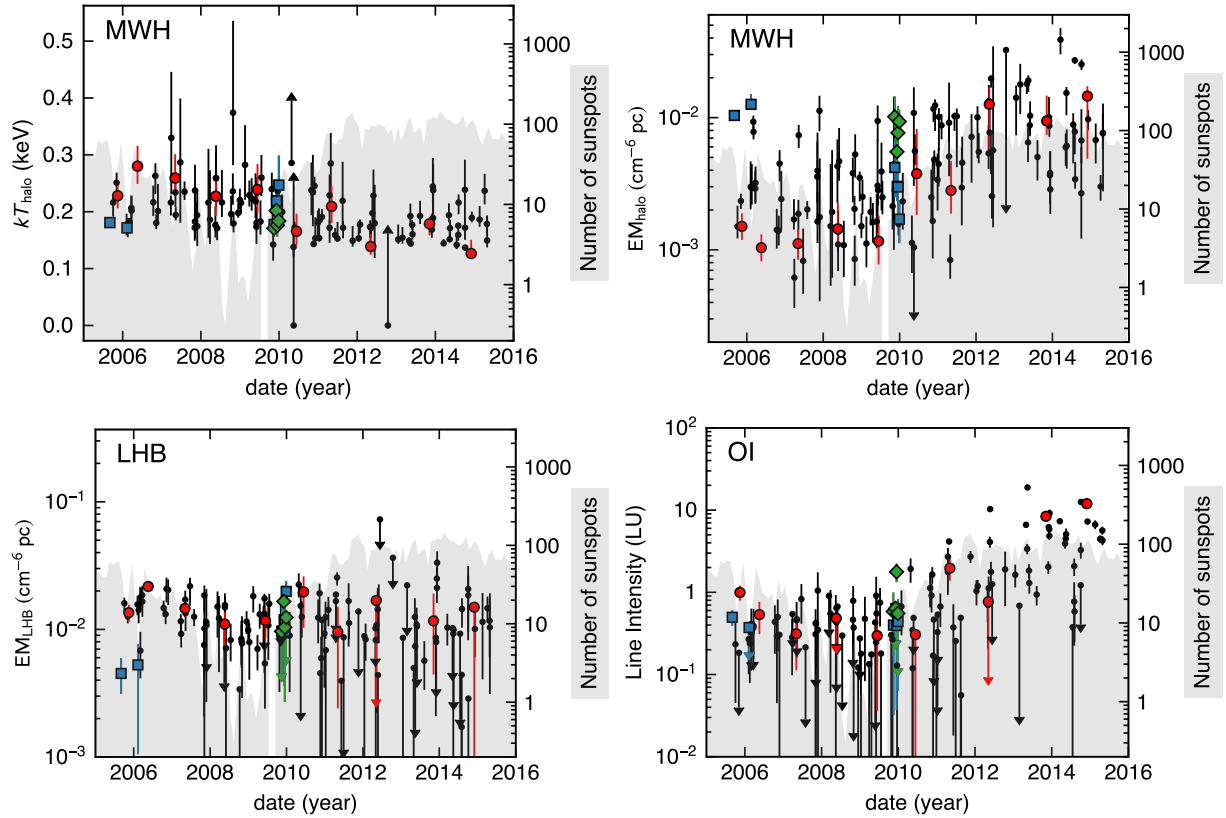


Fig. 5. kT_{halo} and EM_{halo} , the emission measures of the LHB and the normalization of O I, plotted against observation date. Filled circles, filled squares, and filled diamonds correspond to the Lockman Hole, NEP, and SEP, respectively. The gray shaded areas represent the 13-month averaged sunspot number.

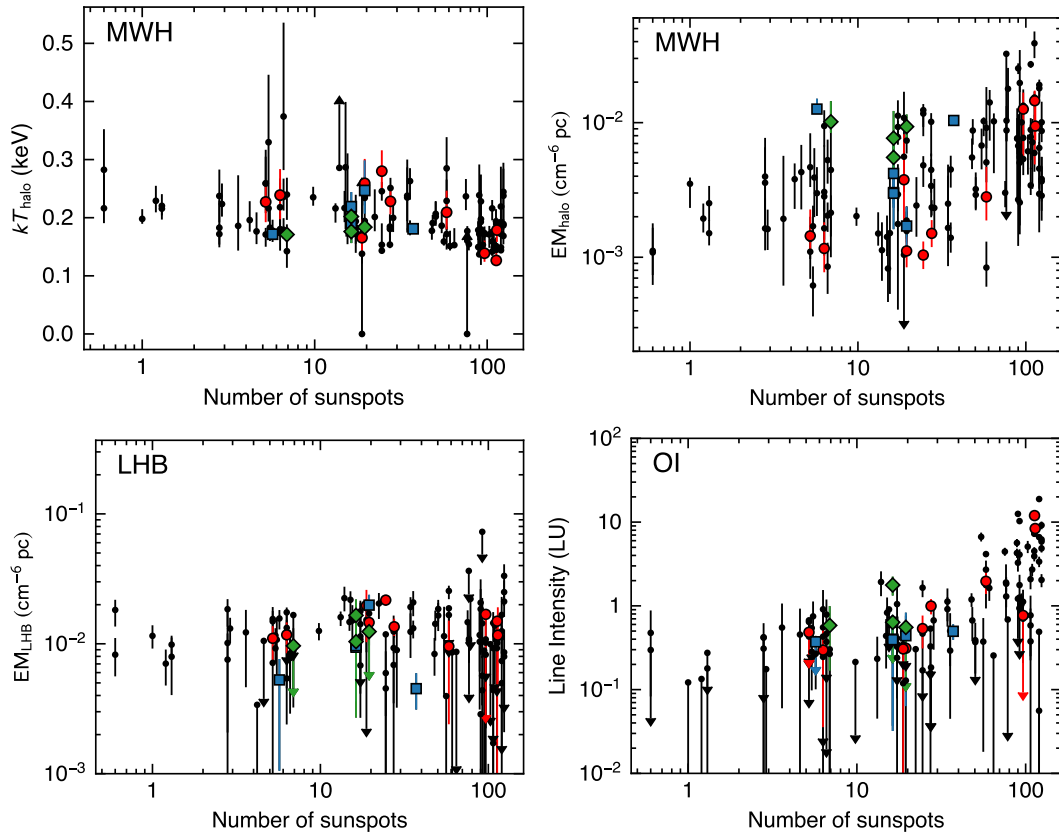


Fig. 6. Same as Figure 5, but plotted against 13-month averaged sunspot number.

Table 2. Medians and 16th-84th percentile ranges of MWH component with Model-08

selection	N*	kT_{halo}		EM_{halo}	
		median (keV)	16th-84th percentile (keV)	median ($10^{-3} \text{ cm}^{-6} \text{ pc}$)	16th-84th percentile ($10^{-3} \text{ cm}^{-6} \text{ pc}$)
all	130	0.19	0.15–0.23	4.0	1.6–10
$kT_{\text{halo}}^{\dagger} \geq 0.19 \text{ keV}$	63	—	—	2.1	1.1–3.8
$kT_{\text{halo}}^{\dagger} < 0.19 \text{ keV}$	67	—	—	7.9	3.9–13
2005–2009	64	0.22	0.18–0.25	2.4	1.4–5.5
2010–2015	66	0.17	0.15–0.23	6.8	2.9–13
$\text{SSN}^{\ddagger} < 20$	49	0.22	0.18–0.25	2.1	1.2–4.8
$20 \leq \text{SSN}^{\ddagger} \leq 50$	30	0.18	0.16–0.25	3.2	1.4–10
$\text{SSN}^{\ddagger} \geq 50$	51	0.17	0.15–0.22	7.7	3.1–15

* Number of observations.

\dagger Temperature of the MWH component.

\ddagger 13 month-averaged sunspot number.

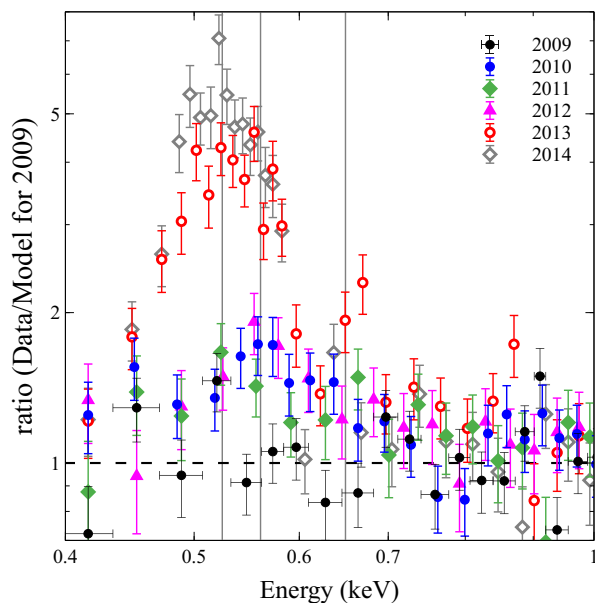


Fig. 7. The ratios of the XIS1 spectra of the Lockman Hole obtained from 2009 to 2014 to the best-fit model for the 2009 observation with Model-08. The three vertical lines indicate the line energies of O I, O VII He α and O VIII Ly α

including the solar minimum around 2009 and the solar maximum around 2014. The overall trend of kT_{halo} and EM_{halo} with Model-08 for the 130 observations seems to depend on the solar activity (figures 5 and 6). At a given epoch, the scatter in these values are relatively small, and most of the derived values are close to those obtained from the Lockman Hole observations. Although we screened the possible geocoronal SWCX emissions using the light curve of each observation, screening the heliospheric one is challenging since the variation time scale is expected to be longer. From the Lockman Hole data with almost the same sightlines, the excess the O VII He α emissions of 3–7 LU (photons $\text{s}^{-1} \text{cm}^{-2} \text{str}^{-1}$) are detected in 2010, 2012–2014

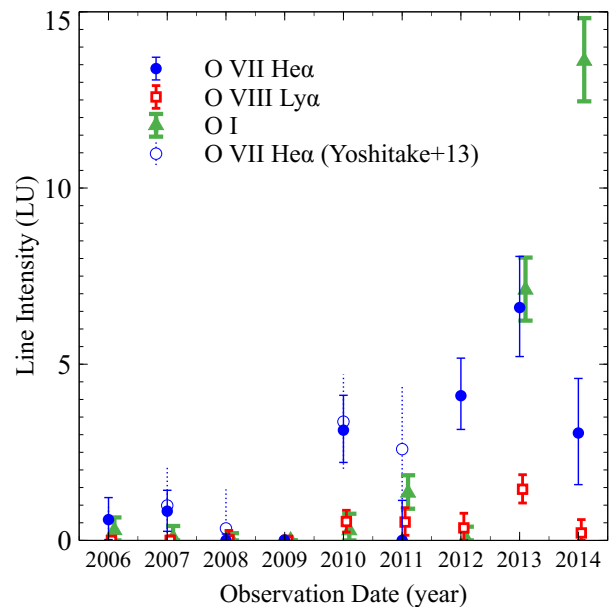


Fig. 8. The normalizations of the Gaussians in units of LU (photons $\text{s}^{-1} \text{cm}^{-2} \text{str}^{-1}$) for the excess emissions of the Lockman Hole data compared to the 2009 data at 0.56 keV (filled circles, O VII He α), 0.65 keV (open squares, O VIII Ly α), and 0.525 keV (filled triangles, O I). The open circles with dotted error bars correspond to the excess O VII He α line strengths compared to the 2009 data obtained by Yoshitake et al. (2013).

compared to the 2009 data. The intensities of the excess O VIII Ly α line are less than 20% of those of O VII He α . The O VII/O VIII line ratios of the excess emission are significantly different from those of the geocoronal SWCX where the strengths of the OVIII line are comparable to those of the O VII line (e.g. Fujimoto et al. 2007; Ishi et al. 2019). Yoshitake et al. (2013) estimated the heliospheric SWCX emission based on the model by Koutroumpa et al. (2006). The predicted intensities of O VII and O VIII lines around the solar maximum are 2.5 LU and 0.8 LU, respectively, and around the solar minimum are 1.7 LU and 0.4 LU, respectively.

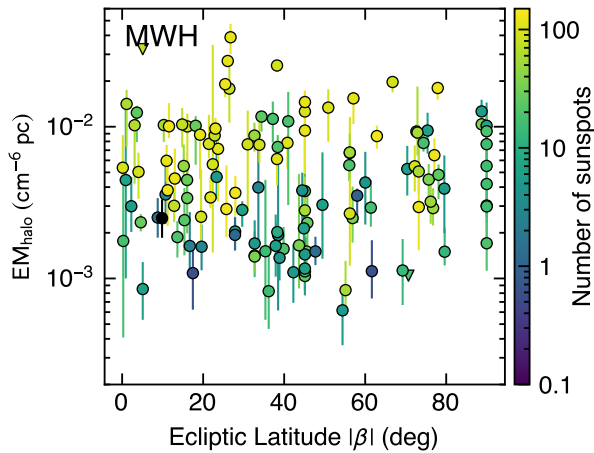


Fig. 9. EM_{halo} plotted against the absolute value of the ecliptic latitude, β . The color scale indicates to the 13 months averaged sunspot number.

With the XMM data covering 10 years, Qu et al. (2022) concluded that the average MWH fluxes are reduced from 10 LU to 5.4 LU for O VII and from 2.5 LU to 1.7 LU for O VIII. These reductions are consistent with the excess O VII and O VIII line strengths obtained from the Lockman Hole data around the solar maximum. These results indicate that the heliospheric SWCX emission, mainly O VII He α line significantly contaminates the spectra obtained around the solar maximum.

Figure 9 shows EM_{halo} of the 130 observations plotted against the absolute value of the ecliptic latitude, with the color scale of the 13 months averaged sunspot number. The heliospheric SWCX is expected to be stronger near the ecliptic plane (Robertson & Cravens 2003; Koutroumpa et al. 2006). When the 13-month averaged sunspot number is larger than several tens, EM_{halo} tends to be high. However, no clear dependence on the ecliptic latitude is seen. Probably, the time variation of the SWCX is much larger than the spatial variation along the ecliptic latitude.

4.2 Correlation between temperature and emission measure of the Milky way halo

The plot of $EM_{\text{halo}}-kT_{\text{halo}}$ shows a negative correlation as shown in figure 10. Most of the 2010-2015 data give higher EM_{halo} and lower kT_{halo} compared to the 2005-2009 data. A CIE component with the temperature of ~ 0.1 keV has been empirically used to represent the emissions from LHB and heliospheric SWCX (e.g. Yoshino et al. 2009, Nakashima et al. 2018). However, contaminations of the emissions related to the solar activity, mainly O VII He α , sometimes cause overestimation of EM_{halo} and underestimation of kT_{halo} , especially around the solar maximum.

Since the emissivity of O VIII depends on the plasma

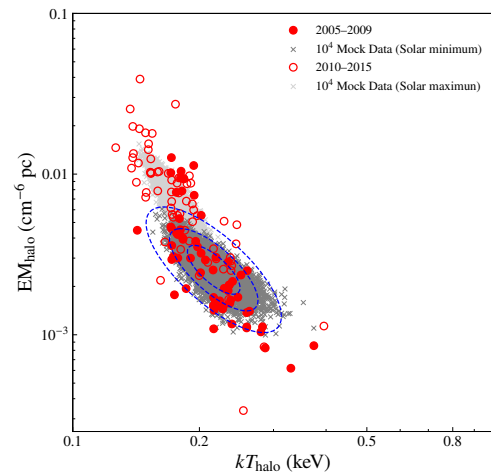


Fig. 10. kT_{halo} plotted against EM_{halo} (closed circles and open circles for the data of 2005-2009 and 2010-2015, respectively) with Model-08. The crosses (dark gray:2005-2009; light gray:2010-2015) shows the best-fit values. The contours indicate the 68%, 90%, and 99% ranges from the mock spectra using the median values for the 2005-2009 data.

temperature, to reproduce the observed O VIII line strengths, there may be some artificial negative correlation between $EM_{\text{halo}}-kT_{\text{halo}}$. To check this effect, we created 10^4 mock XIS spectra with an exposure time of 50 ks and the median values for the 2005-2009 and 2010-2015 data shown in table 2 with Model-08. Figure 10 also shows the best-fit values from the mock spectra with statistical contours. Most of the best-fit values from the 2005-2009 data resemble the distribution from the mock spectra using their median values. In contrast, the scatter for the 2010-2015 data points is larger than that from the corresponding simulations. These results suggest that the negative correlation between EM_{halo} and kT_{halo} is likely artifacts and most of EM_{halo} and kT_{halo} values of the 2005-2009 data are consistent with their median values.

4.3 Comparison with previous results

Figure 11 compares our kT_{halo} vs. EM_{halo} with those by Henley & Shelton (2013) and Nakashima et al. (2018). In order to minimize the contamination by SWCX, Henley & Shelton (2013) analyzed only data after 2005 and $|\beta| > 20^\circ$. They also excluded data around the Orion-Eridanus superbubble (Reynolds & Ogden 1979; Burrows et al. 1993). As a result, their data do not include the highest emission measures which are possibly caused by the contamination of SWCX and by the emission from the bubble. A significant fraction of our data, especially obtained before the end of 2009, is consistent with that by Henley & Shelton (2013). With the HaloSat survey data toward the

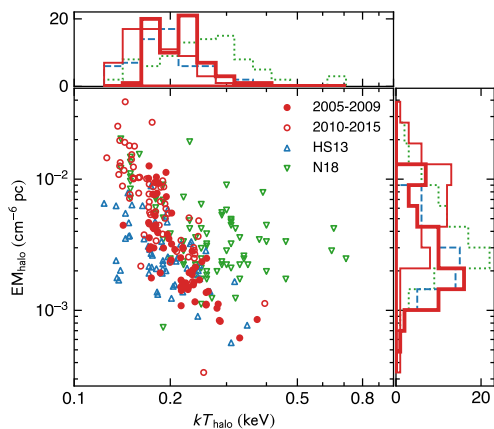


Fig. 11. kT_{halo} plotted against EM_{halo} . The histograms show the distributions of kT_{halo} and EM_{halo} . Closed circles and thick lines are for the 2005-2009 data and open circles and thin lines for the 2010-2015 data with Model-08, open upward triangles and dashed lines are for the data by Henley & Shelton (2013), and open downward triangles and dotted lines are for the data by Nakashima et al. (2018). Here, the effect of the difference in the adopted solar abundance table is corrected.

southern halo ($b < -30^\circ$) obtained around the solar minimum, Kaaret et al. (2020) studied the MWH halo. Their median temperature, 0.225 keV, agrees with our median value. Toward the Galactic anticenter, and high Galactic latitude, their emission measures, $4\text{--}8 \times 10^{-3} \text{ cm}^{-6} \text{ pc}$ (for 0.3 solar gas metallicity) agrees with our median values for the 2005-2009 data, considering the difference in the adopted abundance.

In our analysis, the screening criteria to minimize the SWCX is not as strict as in Nakashima et al. (2018). Nakashima et al. (2018) used a similar variable abundance model with Model-v. Over half of the data are consistent with our work. The other data by Nakashima et al. (2018) show higher kT_{halo} and $[\text{O}/\text{Fe}] \sim 0.5$ to reproduce the residual structure at 0.7–1 keV, while we added the 0.8 keV component to the standard soft X-ray background model. Then, the scatter in kT_{halo} vs. EM_{halo} is significantly reduced from those obtained by Nakashima et al. (2018).

It is reasonable to assume the MWH component extends over the Milky Way considering the small scatter in the kT_{halo} and EM_{halo} of 2005-2009 data, and the residual structure at 0.7–1 keV seen in some regions may be caused by some additional component. The larger C-statistic from the Model-08 fit for the stacked spectra than the Model-v fit is caused by the excess Ne and Mg line emissions at 1 keV and 1.3 keV. There may be another higher temperature component (> 1 keV) or the abundance pattern of the 0.8 keV component may deviate from the solar ratio. We will discuss these possibilities in a different paper

(Sugiyama et al. in preparation).

4.4 Spatial distribution of the Milky Way halo: the disk-like component

Figure 12 shows the sky map of the EM_{halo} with Model-08. Figure 13 shows kT_{halo} and EM_{halo} with the same model fits, plotted against $|l|$ and $|b|$. Here, $|l|$ is defined as l for $0^\circ \leq l < 180^\circ$ and $360^\circ - l$ for $180^\circ \leq l < 360^\circ$. The brightest regions around $l \sim 200^\circ$ and $b \sim -20^\circ, -30^\circ$, and -50° correspond to the Orion-Eridanus superbubble. Except for the regions with $|l| < 105^\circ$ and $|b| < 35^\circ$, kT_{halo} and EM_{halo} are fairly uniform when we adopt the data with the sunspot number less than several tens. Figure 14 shows EM_{halo} for the 2005-2009 data, separated into four $|l|$ ranges. For the data at $|l| > 105^\circ$, the distribution of EM_{halo} is rather smooth, while there is a significant scatter for the data at $|l| < 105^\circ$. For $|b| < 35^\circ$ data, there is an increase of EM_{halo} toward the lower Galactic latitude

The increase of the emission measure towards the low Galactic latitude indicates a presence of a disk-like morphology gas. Yao et al. (2009) proposed a disk-like morphology for the hot gas contributes the soft X-ray background as follows,

$$n_{\text{disk}} = n_0 \exp\left(-\frac{R}{R_0}\right) \exp\left(-\frac{z}{z_0}\right) \quad (1)$$

Here, n_{disk} is the number density, n_0 is the number density at the Galactic center, R is the distance from the Galactic center projected onto the Galactic plane, z is the vertical height from the Galactic disk, and R_0 and z_0 is the scale length and scale height, respectively. The n_0 and z_0 obtained from previous absorption line studies are about $(1\text{--}5) \times 10^{-3} \text{ cm}^{-3}$, and 2–9 kpc (Yao et al. 2009; Hagihara et al. 2010; Sakai et al. 2014). The HaloSat data toward the southern Galactic sky also prefers the disk-like morphology model, with $R_0 = 5.4 \pm 1.5$ kpc, and $z_0 = 2.8 \pm 1.0$ kpc (Kaaret et al. 2020). We fixed R_0 and z_0 at 7.0 kpc and 2.7 kpc, respectively, which are the best-fit values obtained by Nakashima et al. (2018), and fitted the 2005-2009 data. The results are summarized in table 3. However, the fit is unacceptable with a $\chi^2/\text{d.o.f}$ is 389/63. This large χ^2 mainly comes from high EM_{halo} regions at $|l| < 105^\circ$. If we exclude the data with $|l| < 105^\circ$, we obtain a good fit with $\chi^2/\text{d.o.f}=36/35$. Since the O VII line contamination possibly from SWCX causes an underestimate of the temperature, we fitted the data with $kT_{\text{halo}} > 0.2$ keV, including those obtained after 2010. This fit also gives a relatively good fit with $\chi^2/\text{d.o.f}=57/51$. Assuming the solar metallicity, the central electron density from the latter two fits is $(3.4 \pm 0.1) \times 10^{-3} \text{ cm}^{-3}$. However, it is difficult to measure the metal abundance of

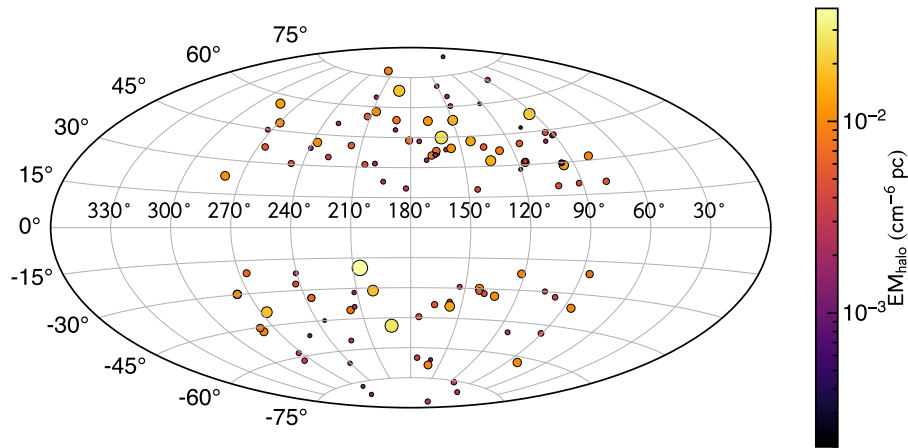


Fig. 12. EM_{halo} across the sky with the galactic coordinates. The color and the size of circles indicate EM_{halo} .

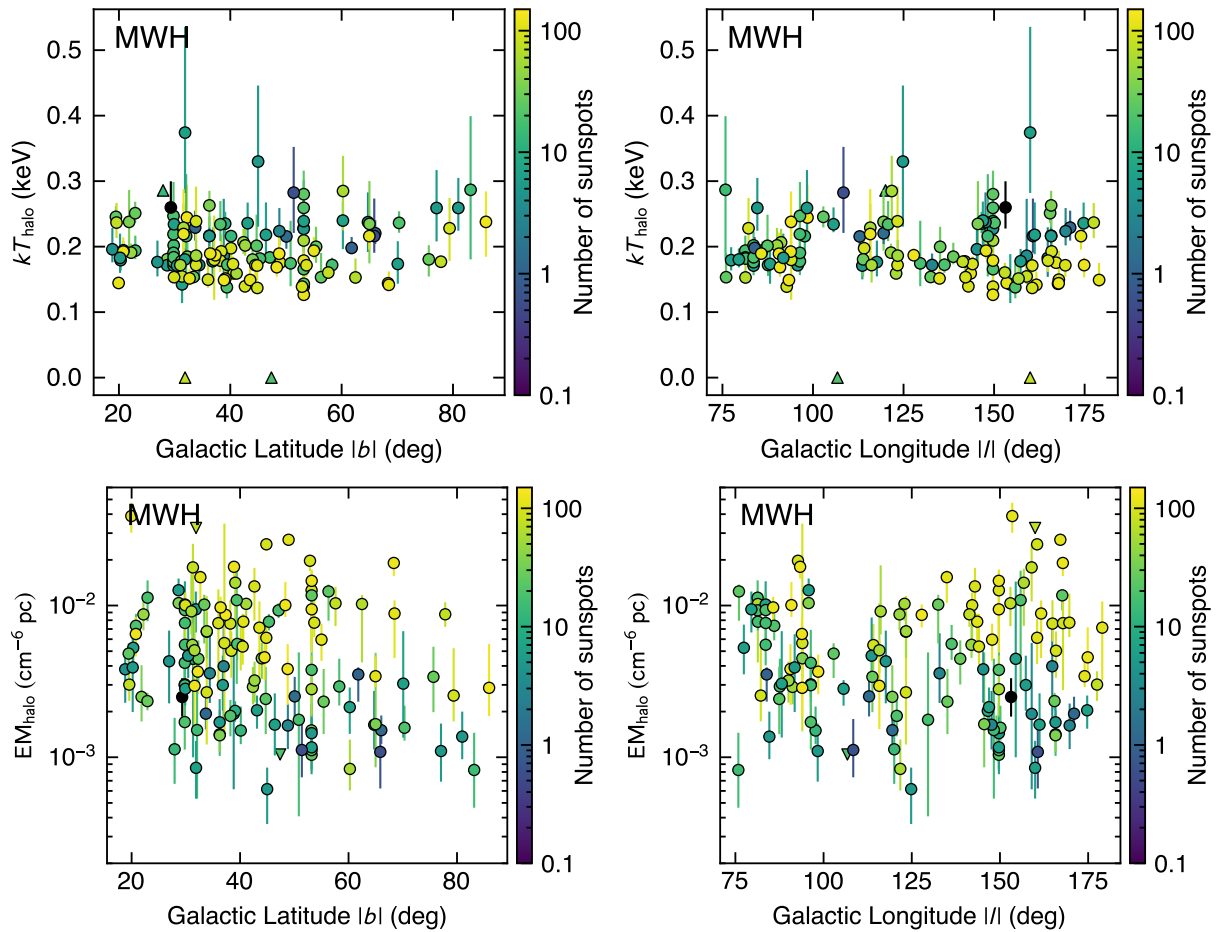


Fig. 13. kT_{halo} and EM_{halo} plotted against the absolute values of the Galactic latitude, $|l|$ and the Galactic longitude, $|b|$. The color scale corresponds to the 13-month-smoothed sunspot number.

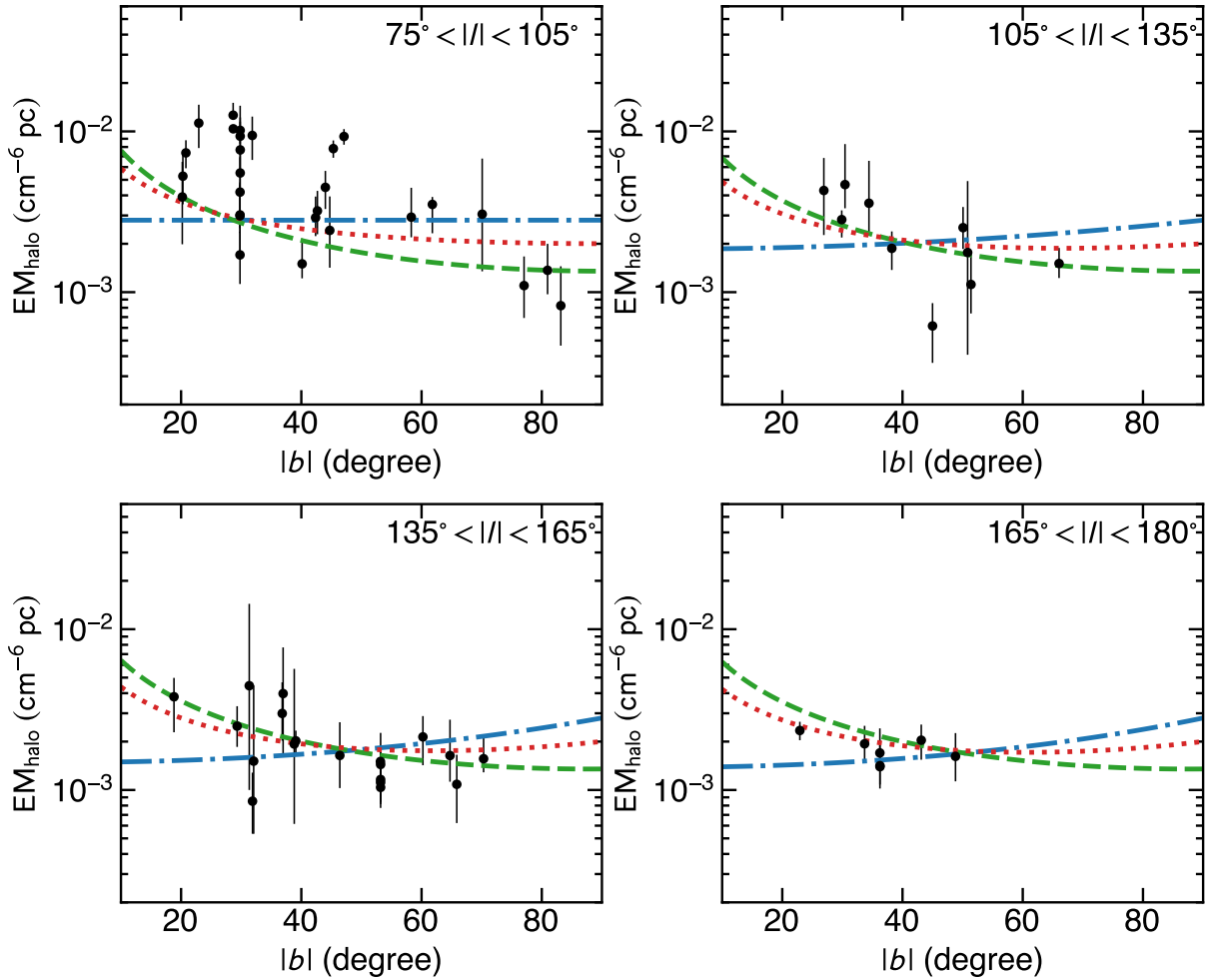


Fig. 14. EM_{halo} for the 2005-2009 data, plotted against the Galactic latitude, $|b|$ (filled circles with error bars). Each panel shows a different range of $|l|$. The dashed, dot-dashed, and dotted lines represent the best-fit disk-like, spherical, and composite models, respectively, at $|l| = 90^\circ, 120^\circ, 150^\circ$, and 180° .

such low-temperature plasma. The derived electron density is roughly inversely proportional to the assumed metallicity. Integrating over this density out to 30 kpc, the gas mass becomes $5 \times 10^8 (Z/0.3 \text{ solar})^{-1} M_\odot$. Here, Z is the metallicity of the hot gas.

This component may be related to the gas heated by supernovae explosions in the stellar disk. Then, the hot gas may relate to star-forming regions, and the emission measures have some scatter. The high EM_{halo} regions at $|l| < 105^\circ$ may be caused by recent stellar feedback. However, the scale height of the SN-driven hot gas ($T > 10^{5.5}$ K) from numerical simulation by Hill et al. (2012), about 0.3–0.5 kpc, is significantly lower than the scale height of 2–9 kpc obtained from the absorption line studies.

4.5 Spatial distribution of the Milky Way halo: the spherical component

Galaxies are thought to be surrounded by a gaseous corona, the CGM. The CGM is expected to consist of mostly hot diffuse gas and contains a significant fraction of baryonic mass. This gas is expected to be heated to the virial temperature and fills the MWH in nearly hydrostatic equilibrium. Numerical simulations indicate that the mass of the CGM is around several percent of the total mass and for the Milky Way, where the expected CGM mass is about $(3\text{--}10) \times 10^{10} M_\odot$ (e.g. Hani et al. 2019; Cautun et al. 2020; Faerman et al. 2022).

The distribution of a hot gas filling a self-gravitating isothermal sphere in hydrostatic equilibrium is often modeled as the β -model,

$$n_{\text{sphere}} = n_c \left(1 + \left(\frac{r}{r_c} \right)^2 \right)^{-3\beta/2}. \quad (2)$$

Here, n_{sphere} is the number density of the gas, n_c is the

Table 3. Fitting results of the density distribution models for MWH

selection	model	N^*	disk		spherical			χ^2/dof
			n_{e0}^\dagger (10^{-3} cm^{-3})	z_0 (kpc)	$M(< 30 \text{ kpc})^\ddagger$ ($10^8 M_\odot$)	n_{ec}^\S (10^{-3} cm^{-3})	$M(< 250 \text{ kpc})^\parallel$ ($10^{10} M_\odot$)	
2005-2009	disk	64	3.9 ± 0.2	2.7	5.6 ± 0.3	—	—	389/63
2005-2009, $ l > 105^\circ$	disk	36	3.4 ± 0.1	2.7	4.9 ± 0.2	—	—	36/35
$kT_{\text{halo}} > 0.2 \text{ keV}$	disk	52	3.4 ± 0.1	2.7	4.9 ± 0.2	—	—	57/51
2005-2009	sphere	64	—	—	—	4.1 ± 0.2	4.2 ± 0.2	439/63
2005-2009, $ l > 105^\circ$	sphere	36	—	—	—	3.6 ± 0.2	3.7 ± 0.2	59/35
$kT_{\text{halo}} > 0.2 \text{ keV}$	sphere	52	—	—	—	3.5 ± 0.1	3.6 ± 0.1	94/51
2005-2009	comp	64	5.9 ± 2.4	0.3	1.0 ± 0.4	2.6 ± 0.9	2.7 ± 0.9	408/62
2005-2009, $ l > 105^\circ$	comp	36	7.8 ± 1.7	0.3	1.3 ± 0.3	$0.9 < 2.1$	$0.9 < 2.2$	32/34
$kT_{\text{halo}} > 0.2 \text{ keV}$	comp	52	7.5 ± 1.2	0.3	1.2 ± 0.2	1.1 ± 0.8	1.1 ± 0.8	52/50

* Number of observations.

\dagger Central electron density and scale height of the disk model, assuming the metal abundance of 1 solar.

\ddagger Integrated gas mass of the disk component within 30 kpc, assuming the metal abundance of 0.3 solar

\S Central electron density of the spherical model, assuming the metal abundance of 1 solar.

\parallel Integrated gas mass of the spherical component within 250 kpc, assuming the metal abundance of 0.3 solar.

core density, r is the distance from the Galactic center, and r_c is the core radius. $\beta = T_{\text{rot}}/T$, where T is the plasma temperature and T_{rot} is from the rotational velocity. Adopting the case with the optically thin O Ly α , the absorption line measurements of our Galaxy indicate $\beta \sim 0.5$ (Miller & Bregman 2015; Bregman et al. 2018). Since the Galaxy's rotation speed corresponds to 0.12 keV, the virial temperature becomes 0.24 keV with $\beta = 0.5$. This temperature is close to the median value of kT_{halo} , 0.22 keV, with Model-08 for the 2005-2009 data. Since our data is not enough to constrain β and r_c from the spatial distribution of EM_{halo} , we fixed them at 0.51 and 2.4 kpc, respectively, following Li & Bregman (2017). Then, integrating emission measure up to the virial radius (250 kpc, Cautun et al. 2020), we fitted the observed EM_{halo} of the 2005-2009 data with equation 2. The results are shown in table 3. Assuming the solar metallicity, the best-fit central electron density is $(4.1 \pm 0.2) \times 10^{-3} \text{ cm}^{-3}$. The integrated gas mass out to the virial radius becomes $4.2 \times 10^{10} (Z/0.3 \text{ solar})^{-1} M_\odot$. Therefore, if the gas metallicity is low, its mass becomes comparable to the expected CGM mass, $5\text{--}6 \times 10^{10} M_\odot$ (Cautun et al. 2020). However, this model yields $\chi^2/d.o.f = 439/63$ and cannot reproduce the data at $|b| < 40^\circ$ and some data at $|l| < 105^\circ$. When we exclude the data at $|l| < 105^\circ$ from the 2005-2009 data or using the data with $kT_{\text{halo}} > 0.2 \text{ keV}$, the spherical model fit gives $\chi^2/d.o.f = 59/35$ and $\chi^2/d.o.f = 94/51$, respectively. These χ^2 values are much larger than those obtained from the disk-like model fits.

4.6 Spatial distribution of the Milky Way halo: the composite model

We then tried a composite model which consists of a disk-like and spherical gas distribution. We assume the density described as

$$n_{\text{comp}} = n_{\text{disk}} + n_{\text{sphere}} \quad (3)$$

In this model, we assume $\beta = 0.51$, $r_c = 2.4 \text{ kpc}$, and $R_0 = 7.0 \text{ kpc}$. We adopt the scale height z_0 at 0.3 kpc. This scale height is consistent with the value expected by numerical simulations by Hill et al. (2012). As shown in figure 14 and table 3, this model also gives a good fit to the 2005-2009 data, except for data with $|l| < 105^\circ$. Assuming the solar metallicity, the best-fit central electron density of the disk and sphere components are $(5.9 \pm 2.4) \times 10^{-3} \text{ cm}^{-3}$ and $(2.6 \pm 0.9) \times 10^{-3} \text{ cm}^{-3}$, respectively. Figure 15 shows the integrated gas mass of the disk and spherical components, assuming 0.3 solar and 1 solar metallicity. The integrated gas mass out to 30 kpc for the disk component and 250 kpc for the spherical component are $(1.0 \pm 0.4) \times 10^8 (Z/0.3 \text{ solar})^{-1} M_\odot$ and $(2.7 \pm 0.9) \times 10^{10} (Z/0.3 \text{ solar})^{-1} M_\odot$, respectively. The latter is comparable to the lower limit of the expected CGM mass. When using the data at $|l| > 105^\circ$ of the 2005-2009 data, or using the data with $kT_{\text{halo}} > 0.2 \text{ keV}$, we get a good fit to the data with the reduced $\chi^2 \sim 1$ (table 3). In these two fits, the gas mass of the spherical component decrease from the previous fit, and its upper limit out to 250 kpc is $\sim 2 \times 10^{10} (Z/0.3 \text{ solar})^{-1} M_\odot$. Even if the spherical component extends out to this radius, most of the emission comes from a distance within a few tens of kpc.

If gas is in hydrostatic equilibrium, the gravitational mass is given by

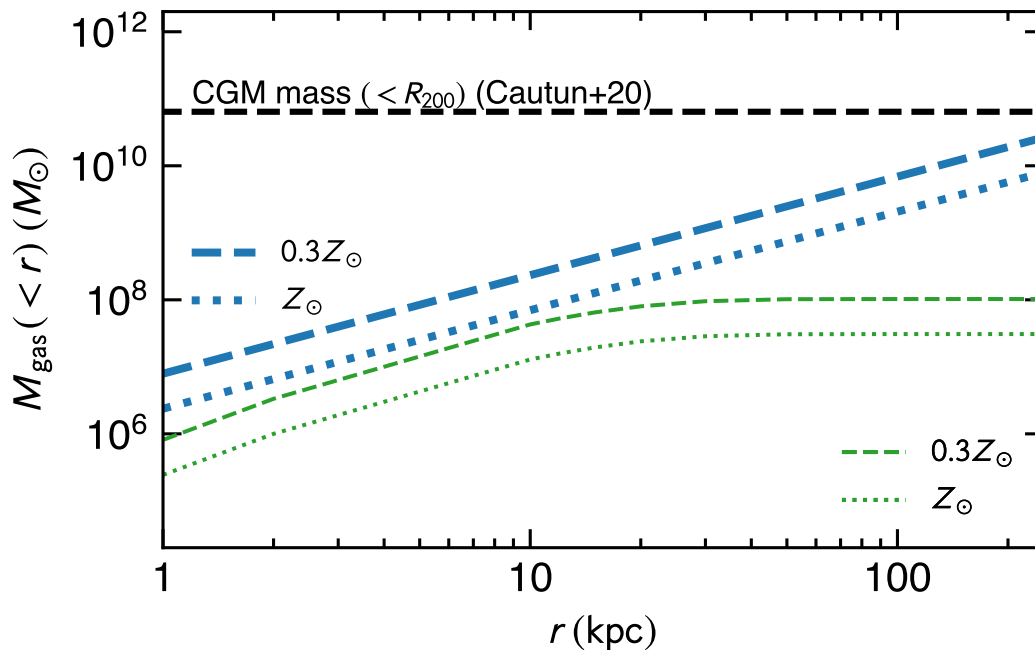


Fig. 15. The integrated gas mass (thick: spherical, thin: disk-like) with the best-fit composite model using the 2005-2009 data. The dashed and dotted lines correspond to the 0.3 solar and 1 solar abundance, respectively. The horizontal dashed line shows the expected CGM mass within R_{200} .

$$M(r) = -\frac{kTr}{\mu m_p G} \left(\frac{d \ln n}{d \ln r} + \frac{d \ln T}{d \ln r} \right) \quad (4)$$

Here, $M(r)$ is the gravitational mass within r , n is the hot gas density, k is the Boltzmann constant, T is the temperature of the gas, μ is the mean molecular weight of 0.61, m_p is the proton mass, and G is the gravitational constant. We adopted the temperature of 0.22 keV and $\beta=0.51$ and calculated the gravitational mass, assuming that the sphere component is in the hydrostatic equilibrium. Figure 16 shows the gravitational mass (hydrostatic mass) calculated out to 30 kpc, beyond which the contribution to the emission measure is minor. The derived hydrostatic mass agrees very well with the total mass of dark matter and baryon obtained by Gaia observations (Cautun et al. 2020).

The accreting gas from outside galaxies is likely in hydrostatic equilibrium, since the expected accretion velocity is low (e.g. Bregman et al. 2018). Our kT_{halo} is fairly uniform at the virial temperature. The smooth distribution of EM_{halo} toward the Galactic anticenter and consistency of the hydrostatic mass and gravitational mass indicate that the hot gas with the virial temperature smoothly fills the halo of the Milky Way, possibly in hydrostatic equilibrium as theoretically expected. However, because of the presence of the disk-like morphology component, it is challenging to constrain the contribution of the spherical component.

5 Summary

We analyzed data of 130 Suzaku observations at $75^\circ < l < 285^\circ$ and $|b| > 15^\circ$ obtained from 2005 to 2015, covering nearly one solar cycle. We exclude time ranges with high count rates to minimize the effect of the geocoronal SWCX. The standard soft X-ray background model consisting of the local hot bubble and the Milky Way Halo (MWH) fails to reproduce a significant fraction of the spectra. We include an additional hot CIE component with a temperature of ~ 0.8 keV to reproduce spectra of a significant fraction of the lines of sight. Then, the scatter in the relation between the EM_{halo} vs. kT_{halo} is reduced. However, the spectra of almost the same lines of sight, for example, the Lockman Hole data, are inconsistent. We simultaneously fitted the nine Lockman Hole spectra obtained from 2006 to 2014 and found an excess O VII He α emission after the solar minimum around 2009. Excess O VIII Ly α is also detected at the solar maximum. These results indicate the heliospheric SWCX emission likely contaminates the spectra and causes underestimation of kT_{halo} and overestimation of EM_{halo} . Adopting the data taken before the end of 2009, at $|b| > 35^\circ$ and $|l| > 105^\circ$, the temperature (~ 0.22 keV) and emission measure ($2 \times 10^{-3} \text{ cm}^{-6} \text{ pc}$) of the MWH are fairly uniform, while at $|b| < 35^\circ$ the emission measure increases toward the lower Galactic latitude. Toward the Galactic anticenter region ($|l| > 105^\circ$), the 2005-2009 data are well represented with a disk-like morphology model and a composite model consisting of a disk

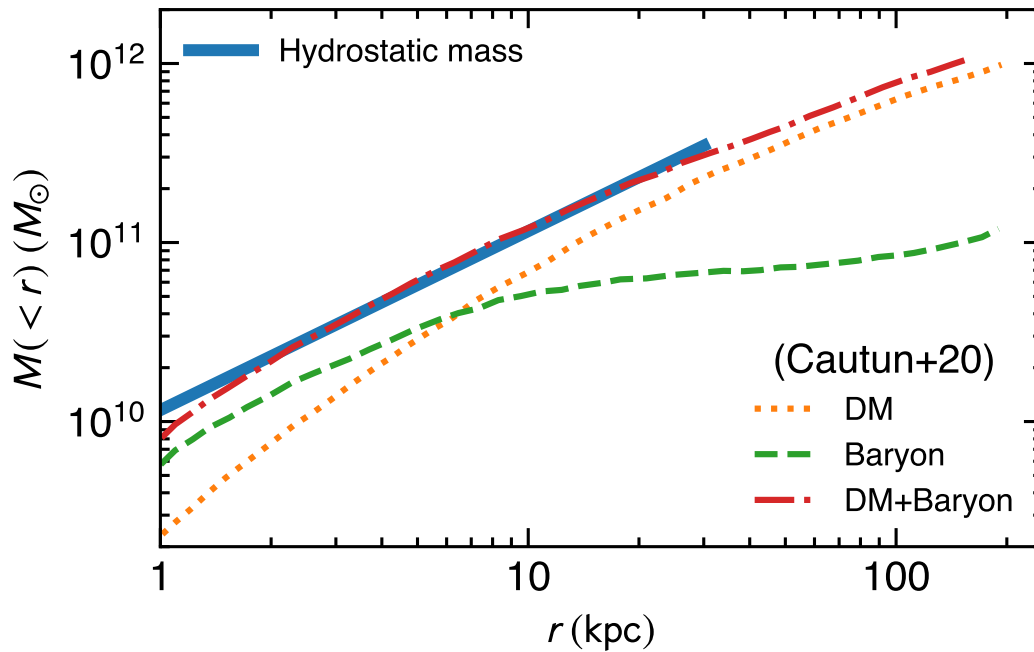


Fig. 16. The integrated hydrostatic mass from the spherical component (solid line). The integrated dark matter (dotted), baryon (dashed), and the sum of dark matter and baryon (dot-dashed) obtained by the Gaia observations (Cautun et al. 2020) are also shown.

and spherical morphology components. The temperature, 0.22 keV, agrees with the virial temperature of the Milky Way. The hydrostatic mass of the spherical component at a few tens of kpc from the Galactic center agrees with the gravitational mass of the Milky Way. These results indicate that the plasma with the virial temperature fills the Milky Way halo with nearly hydrostatic equilibrium. Integrating the density profile of the spherical component out to 250 kpc, or the virial radius, the upper limit of the gas mass of a few $\times 10^{10} M_{\odot}$, assuming 0.3 solar metallicity of the gas. This value is comparable to the lower limit than the expected mass of CGM.

Appendix A Observation log

Suzaku observations used are listed in table 4.

References

- Bregman, J. N., Anderson, M. E., Miller, M. J., et al. 2018, *ApJ*, 862, 3
- Burrows, D. N., Singh, K. P., Nousek, J. A., et al. 1993, *ApJ*, 406, 97
- Carter, J. A., Sembay, S., & Read, A. M. 2010, *MNRAS*, 402, 867
- Cash, W. 1979, *ApJ*, 228, 939
- Cautun, M., Benítez-Llambay, A., Deason, A. J., et al. 2020, *MNRAS*, 494, 4291
- Cravens, T. E., Robertson, I. P., & Snowden, S. L. 2001, *J. Geophys. Res.*, 106, 24883
- Faerman, Y., Pandya, V., Somerville, R. S., et al. 2022, *ApJ*, 928, 37
- Fang, T., Sembach, K. R., & Canizares, C. R. 2003, *ApJL*, 586, L49
- Foster, A. R., Ji, L., Smith, R. K., et al. 2012, *ApJ*, 756, 128
- Fujimoto, R., Mitsuda, K., Mccammon, D., et al. 2007, *PASJ*, 59, 133
- Gupta, A., Kingsbury, J., Mathur, S., et al. 2021, *ApJ*, 909, 164
- Gupta, A., Mathur, S., Kingsbury, J., et al. 2022, arXiv:2201.09915
- Hagihara, T., Yao, Y., Yamasaki, N. Y., et al. 2010, *PASJ*, 62, 723
- Hani, M. H., Ellison, S. L., Sparre, M., et al. 2019, *MNRAS*, 488, 135
- Henley, D. B. & Shelton, R. L. 2013, *ApJ*, 773, 92.
- Hill, A. S., Joung, M. R., Mac Low, M.-M., et al. 2012, *ApJ*, 750, 104.
- Ishi, D., Ishikawa, K., Numazawa, M., et al. 2019, *PASJ*, 71, 23
- Ishisaki, Y., Maeda, Y., Fujimoto, R., et al. 2007, *PASJ*, 59, 113
- Kaaret, P., Koutroumpa, D., Kuntz, K. D., et al. 2020, *Nature Astronomy*, 4, 1072. doi:10.1038/s41550-020-01215-w
- Kalberla, P. M. W., Burton, W. B., Hartmann, D., et al. 2005, *A&A*, 440, 775
- Koyama, K., Tsunemi, H., Dotani, T., et al. 2007, *PASJ*, 59, 23
- Koutroumpa, D., Lallement, R., Kharchenko, V., et al. 2006, *A&A*, 460, 289
- Koutroumpa, D., Acero, F., Lallement, R., et al. 2007, *A&A*, 475, 901
- Kuntz, K. D. & Snowden, S. L. 2000, *ApJ*, 543, 195
- Li, Y. & Bregman, J. 2017, *ApJ*, 849, 105
- Lodders, K. 2003, *ApJ*, 591, 1220

- Miller, M. J. & Bregman, J. N. 2015, *ApJ*, 800, 14
- Nakashima, S., Inoue, Y., Yamasaki, N., et al. 2018, *ApJ*, 862, 34.
- Nicastro, F., Zezas, A., Drake, J., et al. 2002, *ApJ*, 573, 157
- Reynolds, R. J. & Ogden, P. M. 1979, *ApJ*, 229, 942
- Rees, M. J. & Ostriker, J. P. 1977, *MNRAS*, 179, 541
- Robertson, I. P. & Cravens, T. E. 2003, *Journal of Geophysical Research (Space Physics)*, 108, 8031
- Sakai, K., Yao, Y., Mitsuda, K., et al. 2014, *PASJ*, 66, 83
- Sekiya, N., Yamasaki, N. Y., Mitsuda, K., et al. 2014a, *Suzaku-MAXI 2014: Expanding the Frontiers of the X-ray Universe*, 66
- Sekiya, N., Yamasaki, N. Y., Mitsuda, K., et al. 2014b, *PASJ*, 66, L3
- Snowden, S. L., Egger, R., Finkbeiner, D. P., et al. 1998, *ApJ*, 493, 715
- Smith, R. K., Brickhouse, N. S., Liedahl, D. A., et al. 2001, *ApJL*, 556, L91
- Tawa, N., Hayashida, K., Nagai, M., et al. 2008, *PASJ*, 60, S11.
- Tumlinson, J., Peebles, M. S., & Werk, J. K. 2017, *ARA&A*, 55, 389
- Yao, Y., Wang, Q. D., Hagihara, T., et al. 2009, *ApJ*, 690, 143
- Yoshino, T., Mitsuda, K., Yamasaki, N. Y., et al. 2009, *PASJ*, 61, 805
- Yoshitake, H., Sakai, K., Mitsuda, K., et al. 2013, *PASJ*, 65, 32
- Qu, Z., Koutroumpa, D., Bregman, J. N., et al. 2022, *ApJ*, 930, 21

Table 4. Suzaku Observation log

Sequence*	Target Name	l †	b ‡	N_{H} §	date	Exposure Time (ks)
100018010	NEP	95.74	28.67	4.0	2005/09/02	93.8
100030020	A2218offset	97.71	40.11	2.4	2005/10/02	43.1
100046010	LOCKMANHOLE	148.97	53.13	0.6	2005/11/14	68.1
101002010	LOCKMANHOLE	149.71	53.22	0.6	2006/05/17	72.9
102018010	LOCKMANHOLE	149.73	53.20	0.6	2007/05/03	88.3
103009010	LOCKMANHOLE	149.71	53.22	0.6	2008/05/18	83.4
104002010	LOCKMANHOLE	149.71	53.22	0.6	2009/06/12	92.8
105003010	LOCKMANHOLE	149.72	53.22	0.6	2010/06/11	71.3
106001010	LOCKMANHOLE	149.73	53.21	0.6	2011/05/04	40.3
107001010	LOCKMANHOLE	149.74	53.20	0.6	2012/05/05	32.2
108001010	LOCKMANHOLE	149.66	53.18	0.6	2013/11/06	36.0
109014010	LOCKMANHOLE	149.66	53.17	0.6	2014/11/30	30.2
402044010	SW UMA	164.79	36.95	4.1	2007/11/06	16.8
402046010	BZ UMA	159.03	38.83	4.8	2008/03/24	25.1
402089020	TW HYA	278.66	22.96	6.8	2007/11/25	19.3
403008010	AM HERCULES BGD	77.40	20.27	6.5	2008/11/01	40.5
403039010	ASAS J002511+1217.2	112.94	-50.08	5.7	2009/01/10	28.9
404035010	HD72779	205.49	31.34	2.9	2009/11/06	65.2
405014010	PSR J0614-33	240.49	-21.83	3.9	2010/10/29	27.6
405034010	EG AND	121.56	-22.18	13.0	2011/02/05	90.7
406007010	1FGL J2339.7-0531	81.33	-62.46	3.2	2011/06/29	95.2
407039010	EUVE J1439 +75.0	114.11	40.15	3.3	2012/05/20	28.3
407043010	CH UMA	142.92	42.67	4.7	2012/05/01	45.2
407045010	BF ERI	201.05	-31.29	5.8	2013/02/27	30.7
408029010	V1159 ORI	206.54	-19.93	27.6	2014/03/16	192.0
408030010	SWIFT J2319.4+2619	98.49	-32.24	6.8	2013/12/07	38.2
409029010	1RXS J032540.0-08144	192.85	-48.96	5.9	2014/07/31	37.3
409030010	IW ERIDANI	216.42	-40.63	2.8	2014/08/01	39.8
500026010	NEP	95.81	28.67	4.0	2006/02/10	80.5
500027020	HIGH LAT. DIFFUSE B	272.41	-58.26	3.3	2006/02/17	103.6
501001010	SKY50.0-62.4	278.68	-47.07	2.4	2006/03/01	79.1
501002010	SKY53.3-63.4	278.63	-45.3	5.8	2006/03/03	101.5
501004010	DRACO HVC REGION A	91.22	42.39	1.8	2006/03/20	57.3
501005010	DRACO HVC REGION B	90.09	42.69	1.5	2006/03/22	57.3
501101010	DRACO ENHANCEMENT	93.99	43.97	1.1	2006/11/09	68.7
501104010	MBM12 OFF-CLOUD	157.36	-36.82	9.0	2006/02/06	72.1
502047010	LOWLATITUDE86-21	86.00	-20.77	7.9	2007/05/09	79.6
502076010	ERIDANUS HOLE	213.42	-39.10	2.6	2007/07/30	95.8
503104010	ARCBACKGROUND	240.49	-66.01	4.1	2008/12/30	176.4
504062010	VICINITY OF NGC 4051	150.12	70.29	1.2	2009/12/19	84.0
504069010	SEP #1	276.39	-29.82	5.8	2009/11/14	51.9
504070010	NEP #1	96.38	29.78	4.5	2009/11/15	52.2
504071010	SEP #2	276.38	-29.82	5.8	2009/12/05	58.0
504072010	NEP #2	96.40	29.78	4.5	2009/12/07	43.6
504073010	SEP #3	276.38	-29.82	5.8	2009/12/14	44.4
504074010	NEP #3	96.40	29.78	4.5	2009/12/15	45.7
504075010	SEP #4	276.38	-29.81	5.8	2009/12/27	49.7
504076010	NEP #4	96.42	29.79	4.5	2009/12/28	49.6

Table 4. (Continued)

Sequence*	Target Name	l †	b ‡	N_H §	date	Exposure Time (ks)
505044010	L139B-32	138.78	-32.31	6.9	2011/01/08	78.9
505058010	L168B53	167.63	53.18	0.9	2010/11/19	77.7
506024010	3C 59 VICINITY 1	142.15	-29.91	7.2	2012/01/14	48.9
506025010	3C 59 VICINITY 2	141.97	-31.19	6.6	2012/01/26	156.6
506056010	G236+38 OFF	237.09	41.12	2.1	2011/06/07	68.0
508073010	MBM16-OFF	165.84	-38.39	19.0	2013/08/09	77.4
509008010	HOT BLOB 2	164.91	38.21	3.2	2015/04/25	72.9
509009010	HOT BLOB 3	167.90	36.02	5.0	2015/04/27	75.9
700011010	SWIFT J0746.3+2548	194.50	22.91	5.1	2005/11/04	88.8
701008010	IRASF11223-1244	272.53	44.75	4.8	2006/11/25	33.5
701057010	APM 08279+5255	165.73	36.24	4.7	2006/10/12	92.4
701057020	APM 08279+5255	165.73	36.23	4.7	2006/11/01	90.9
701057030	APM 08279+5255	165.78	36.24	4.7	2007/03/24	105.8
702031010	MRK 1239	239.29	38.22	4.4	2007/05/06	57.9
702062010	Q0450-1310	211.76	-32.06	10.3	2008/03/10	15.3
702064010	Q1017+1055	230.34	50.84	3.4	2007/11/27	17.5
702076010	SWIFT J0918.5+0425	227.08	34.42	3.8	2007/11/04	54.4
702115010	IRAS 10565+2448	212.31	64.73	1.1	2007/11/06	36.6
703002010	PKS0208-512	276.08	-61.77	1.9	2008/12/14	48.7
703003010	Q0827+243	200.00	31.88	3.3	2008/10/27	44.8
703008010	SWIFT J0911.2+4533	174.69	43.11	1.3	2008/10/25	85.9
703016010	SWIFT J0134.1-3625	261.76	-77.07	2.1	2008/05/20	34.9
703036020	Q0551-3637	242.39	-26.93	3.6	2008/05/14	21.6
703037010	Q0109-3518	275.54	-80.97	2.0	2008/05/20	30.0
703040010	Q0940-1050	246.41	30.44	4.6	2008/05/30	29.9
703042010	J081618.99+482328.4	171.04	33.70	5.8	2009/03/27	80.5
703062010	NGC 1448	251.61	-51.36	1.0	2009/02/17	45.2
703065010	IRASF01475-0740	160.66	-65.86	2.2	2008/07/14	53.8
704008010	1739+518	79.52	31.87	3.1	2009/06/03	22.5
704013010	2MASX J02485937+2630	153.12	-29.32	15.2	2009/07/18	37.1
704014010	UGC 12741	105.64	-29.87	7.9	2009/06/07	45.7
704039010	PKS 0326-288	224.92	-55.38	1.0	2010/01/30	52.2
704048010	NGC 3718	146.85	60.20	1.1	2009/10/24	42.9
704050010	SDSS J1352+4239	88.09	70.11	1.0	2009/06/02	29.5
704052010	SDSS J0943+5417	161.24	46.43	1.5	2009/05/24	32.1
704053010	IC 2497	190.29	48.82	1.1	2009/04/18	74.4
705001010	MRK 18	155.88	39.41	5.0	2010/05/14	35.5
705003010	1150+497	145.50	64.96	2.2	2010/11/12	99.7
705012010	EMS1160	120.04	27.95	8.6	2010/04/26	20.3
705023010	LEDA 84274	106.76	47.41	1.3	2010/05/15	49.5
705024010	IRAS 01250+2832	132.53	-33.41	8.2	2011/01/10	51.2
705027010	EMS1341	102.86	19.43	21.0	2010/11/27	21.3
705045010	IRAS 12072-0444	283.96	56.33	3.5	2010/12/04	56.3
705046010	IRAS 00397-1312	113.94	-75.67	1.8	2010/12/28	78.4
705054010	NGC 3147	136.30	39.49	3.3	2010/05/24	132.5
706004010	NGC6251LOBEBGD1	116.19	31.06	7.9	2011/04/16	17.5
706005010	NGC6251LOBEBGD2	115.83	31.62	6.0	2011/04/16	10.9

Table 4. (Continued)

Sequence*	Target Name	l †	b ‡	N_H §	date	Exposure Time (ks)
706005020	NGC6251LOBEBGD2	115.77	31.62	6.0	2011/08/16	11.2
706013010	3C78	174.83	-44.51	14.6	2011/08/20	91.2
706037010	MRK 231	121.78	60.27	1.0	2011/04/27	192.1
706038010	IRAS 09104+4109	180.98	43.54	1.5	2011/11/18	77.4
707006010	3C 236 BACKGROUND	190.38	53.69	1.0	2012/05/08	42.2
707007010	2FGL J0923.5+1508	215.99	40.48	3.2	2012/04/29	86.0
707008010	2FGL J1502.1+5548	92.72	52.92	1.4	2012/05/22	60.5
707009010	2FGL J0022.2-1853	82.11	-79.36	2.1	2012/05/30	34.3
707012010	NGC 3431	266.05	37.09	4.8	2012/06/11	54.7
707021010	AO 0235+164	156.79	-39.11	10.3	2013/01/18	39.4
707041010	0827+243	200.00	31.87	3.3	2012/10/13	7.9
708002010	NGC 3997	218.79	77.83	7.1	2013/05/27	80.6
708004010	ESO 119-G008	266.69	-38.88	1.3	2013/04/29	97.2
708023010	MRK533	90.64	-48.80	5.2	2013/12/08	50.2
708026010	NGC 235A	94.33	-85.93	1.5	2013/12/10	19.6
708038010	IRAS F11119+3257	192.25	68.36	2.2	2013/05/13	241.3
708039010	VII ZW 403	127.83	37.30	3.9	2013/12/01	81.8
708043010	NGC 3660	269.08	48.37	4.0	2013/11/28	121.8
708044010	B2 1023+25	207.08	57.61	1.7	2013/05/30	93.7
709003010	NGC 2655	134.95	32.71	2.4	2014/05/12	72.2
709004010	SWIFT J2248.8+1725	85.73	-36.43	7.7	2014/12/06	73.0
709007010	SWIFT J0714.2+3518	182.51	19.57	6.7	2015/04/04	72.9
709009010	ARP318	173.93	-64.98	2.8	2014/08/04	74.0
709019010	Q0142-100	161.6	-68.48	3.2	2014/07/16	56.7
709020010	HE0512-3329	236.62	-33.86	2.6	2014/10/02	6.5
709020020	HE0512-3329	236.62	-33.86	2.6	2014/10/03	26.5
709020030	HE0512-3329	236.63	-33.84	2.6	2015/02/18	24.7
709021010	I ZW 18	160.55	44.86	2.7	2014/05/15	16.5
709021020	I ZW 18	160.49	44.84	2.7	2014/10/04	72.9
802083010	COMABKG	75.61	83.17	1.0	2007/06/21	29.8
803041010	NGC1961BACKGROUND	145.24	18.80	13.1	2008/10/09	23.1
808057010	BULLET-BKG	266.17	-20.77	6.8	2013/05/10	48.9
809052010	OFF-FIELD1	212.28	55.01	2.1	2014/05/05	36.6
901005010	GRB070328	235.21	-44.99	2.9	2007/03/28	50.4
904001010	GRB 090709A	91.78	20.22	8.5	2009/07/09	58.4

* Sequence numbers of the Suzaku archive.

† Galactic longitude in units of degrees.

‡ Galactic latitude in units of degrees.

§ Galactic hydrogen column density in units of 10^{20}cm^{-2}

|| Observation start date.